Clustering and properties of $K-$band companion galaxies around USS radio sources[*].

Carlos G. Bornancini[1], Diego G. Lambas[1,2] Carlos De Breuck[3].

[1] *Grupo de Investigaciones en Astronomía Teórica y Experimental, IATE*
Observatorio Astronómico, Universidad Nacional de Córdoba
Laprida 854, X5000BGR, Córdoba, Argentina.
[2] *Consejo Nacional de Investigaciones Científicas y Técnicas (CONICET), Avenida Rivadavia 1917, C1033AAJ, Buenos Aires, Argentina.*
[3] *European Southern Observatory, Karl Schwarzschild Straße 2, D-85748 Garching, Germany.*

5 February 2008

ABSTRACT

We have analyzed galaxy properties in the environment of a sample of 70 Ultra Steep Spectrum (USS) radio sources selected from the Sydney University Molonglo sky Survey and the NRAO VLA Sky Survey catalogues, using near-IR data complete down to $K_s = 20$. We have quantified galaxy excess around USS targets using an Abell–type measurement $N_{0.5}$ (Hill & Lilly 1991). We find that most of the USS fields studied are compatible with being Abell class 0 richness clusters. A statistical analysis of the distribution of companion galaxies around USS radio sources show a pronounced tendency for such objects to be found in the direction defined by the radio axis, suggesting that they may be related to the presence of the radio sources. We have also measure the central concentration of light of the USS sample and compare these to the values obtained for field galaxies and galaxies selected through other methods. By using Spearman statistics to disentangle richnesses and concentration indices dependences, we detect a weak, but significant, positive correlation. We find that at $z > 2$ USS radio sources are more concentrated than field galaxies at similar redshifts, indicating that these objects trace the most massive systems at high redshift.

Key words: cosmology: large-scale structure of Universe–galaxies: clusters: general – galaxies: high-redshift.

1 INTRODUCTION

Hierarchical galaxy formation models predicts that large galaxies and other massive structures, grow from mergers of small subunit of mass. Studying the properties of distant clusters of galaxies and their evolution can directly constrain theories of galaxy evolution and cosmological models (Bahcall & Fan 1998). High redshift radio galaxies are ideal targets to find the most massive galaxies at a given redshift. Radio galaxies follow a close relation in the Hubble $K - z$ diagram (Lilly & Longair 1984). At $z \gtrsim 1$ they are $\gtrsim 2$ magnitudes brighter than normal galaxies at these redshifts (De Breuck et al. 2002), and can be used to find the most luminous star-forming populations. Using galaxy evolution models, Rocca-Volmerange et al.

(2004), find that the brightest luminosity limit of the Hubble K diagram for typical powerful radio galaxies, correspond to the most massive elliptical galaxies of $\sim 10^{12} M_\odot$. One of the most successful technique to find high redshift radio galaxies, has been the ultra steep spectrum criterion (USS) (Röttgering et al. 1994; Chambers et al. 1996a; Blundell et al. 1998). Selecting sources with steep radio spectra ($\alpha \lesssim -1.30; S_\nu \propto \nu^\alpha$) increases dramatically the chance of finding $z > 2$ radio galaxies (Röttgering et al. 1994; Chambers et al. 1996b; Jarvis et al. 2001). It has been known for some time that USS radio galaxies share a close relationship with groups and clusters of galaxies (Chambers et al. 1996a; Knopp & Chambers 1997). From cross–correlation analysis (Bornancini et al. 2004a), there is evidence that USS sources at redshift ~ 1 are located in cluster environments, comparable to that expected for clusters of Abell richness class 0 (Best 2000; Best et al. 2003). Recently, the search for distant forming clusters of galaxies (proto–clusters) associated with radio galaxies has made

significant progress in our knowledge of the large-scale structure at high redshifts (Pentericci et al. 1997; Kurk et al. 2000; Venemans et al. 2002; Miley et al. 2004). Some high redshift radio galaxies show very close companion objects along the radio axis. Röttgering et al. (1996), find a statistical excess of optical companion galaxies up to ~ 80 kpc distance along the radio axis of USS radio sources. Pentericci et al. (2001) reported a similar effect, finding faint close companion galaxies along the radio axis. Croft et al. (2005) found evidence for a filamentary structure associated with the radio galaxy MRC 1138-262 at $z = 2.16$, consisting in a number of X–ray sources (Pentericci et al. 2002), Lyα emitters (Pentericci et al. 2000), Hα emitters (Kurk et al. 2004a) and EROs (Kurk et al. 2004b) at redshifts close to that of the radio source, aligned with the axis of the radio emission of the central galaxy.

In this paper we analyze galaxy clustering and surrounding galaxy properties around a large sample of USS radio sources by studying an Abell-type measurement $N_{0.5}$. We examine the dependence on the environmental variations and radio and/or IR source properties, such as the radio size, position angle of the radio structure and central concentration indices and the evolution with redshift. This paper is organized as follows: Section 2 describes the sample of analyzed, the source extraction, the completeness of the sample and photometry techniques. We quantify galaxy excess associated to USS radio galaxies in Section 3. We investigate the statistics of aligned companion galaxies respect to the radio axis of USS targets in Section 4. In section 5, we investigate the central light concentration of USS targets. Finally we discuss our results in Section 6.

Unless otherwise stated, we will use a flat cosmology with density parameters $\Omega_M = 0.3$, $\Omega_\Lambda = 0.7$ and a Hubble's constant $H_0 = 100\ h$ kms^{-1} Mpc^{-1}.

2   DATA ACQUISITION

The USS sample selection and radio data used for this analysis was presented and described by De Breuck et al. (2004). In short, we used the pre-release version of the SUMSS catalogue and the version 39 of the NVSS catalogue to construct and select a sample of Ultra Steep Spectrum sources. We used the Australia Telescope Compact array (ATCA) to measure radio morphologies and accurate radio positions. We used 70 radio sources restricted to have an ultra steep radio continuum spectrum, with 53 sources with a spectral index cutoff $\alpha_{843}^{1400} < -1.3$ and 17 sources with $\alpha_{843}^{1400} > -1.3$. We have decided to retain these 17 sources in order to search correlations with other radio and/or IR properties. The near-IR data used in this work were obtained using the `IRIS2` instrument at the 3.9m Anglo-Australian Telescope at Siding Spring Observatory. Conditions were mostly photometric with FWHM $\sim 2''$. A K_s filter was used. The pixel size was $0''446$/pixel, resulting in a respective $\sim 8' \times 8'$ field of view. For the 20 sources not detected in the AAT/IRIS2 images, we obtained deeper K_s–band images using the Son of Isaac (Sofi) instrument at the ESO 3.5m New Technology Telescope (NTT). Conditions were photometric with $\sim 0''7$ seeing. The pixel size was $0''292$/pixel, resulting in a respective $\sim 5' \times 5'$ field of view. The galaxy sample used in this work consist in galaxies identified in 50 images obtained with the AAT telescope and 20 deeper USS fields obtained with NTT telescope. A full description of sample selection, observations and image reductions is given in De Breuck et al. (2004).

2.1   Photometry and Catalogue Creation

For object detection and photometry we used the v2.2.2 of the SExtractor software package (Bertin & Arnouts 1996). For the AAT and NTT images, the source extraction parameters were set such that, to be detected, an object must have a flux in excess of 1.5 times the local background noise level over at least N connected pixels, according to the seeing conditions (~ 5 and ~ 8 pixels for AAT and NTT images, respectively). Four and six USS sources weren't detected with this detection threshold in the ATT and NTT images, respectively.

SExtractor's `MAG_BEST` estimator was used to determine the magnitudes of the sources. In this work we choose all objects (galaxies) with stellaricity index < 0.8, for the AAT images and < 0.9 for the NTT images.

The result of the detection process was inspected visually in order to ensure that no obvious objects were missed, and that no false detections were entered into the catalogues. Saturated objects and objects lying in the image boundaries were rejected from the catalogues.

Our sample sources is listed in Table 1 and Table 2 in IAU J2000 format, together with the spectral index α_{843}^{1400}, position angle of the radio structure determined from the ATCA maps, largest radio size (LAS), the K_s counterpart magnitude, the Hill & Lilly quantity $N_{0.5}$, the corrected central concentration, the spectroscopic redshift (De Breuck et al. 2005) and the expected redshift, estimated from the $K - z$ Hubble Diagram and the 1.5 σ limiting magnitude per field.

2.2   Monte-Carlo test of completeness

In order to investigate the accuracy of the total magnitudes, the complete level of the source extraction (deblending) and set the appropriate value of the K_s–magnitude limit for inclusion in our sample, we have produced a Monte-Carlo test.

A series of model galaxies and stars was made using the IRAF[1] ARTDATA `mkobjects` task with typical magnitudes, sizes, redshifts and Poisson noise, similar than our images. We created 20 artificial images with 30% of the galaxies represented by a de Vaucouleurs's law and 70% with an exponential disk surface brightness law. The model objects were then convolved with a Gaussian function representing the PSF effects. SExtractor was run on the original and to the convolved model images to determine the differences between input and observed due to the effects before mentioned. In Figure 1, we plot the input and measured magnitudes of each detected object in the simulations (Left panel) and the scatter of the measured magnitudes as a function of input magnitudes (Right panel). We find low scatter generally at at bright magnitudes. At faint magnitudes we find

---

[1] Image Reduction and Analysis Facility (IRAF), a software system distributed by the National Optical Astronomy Observatories (NOAO).
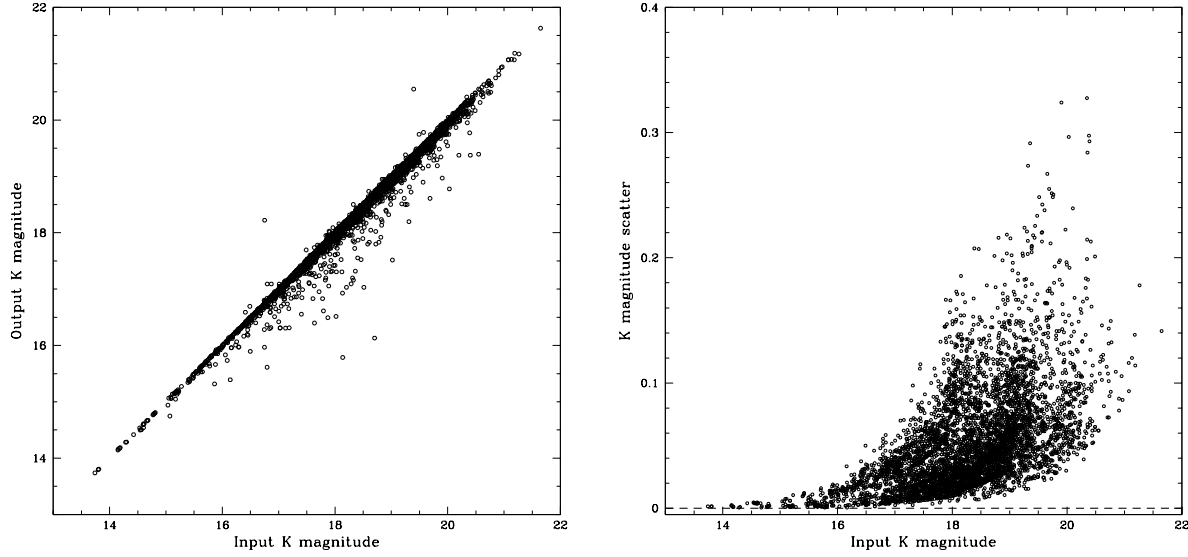
Figure 1. The distribution of measured magnitudes (output) as a function of input magnitudes (Left panel). RMS scatter as a function of input magnitudes (Right panel), for the AAT images.
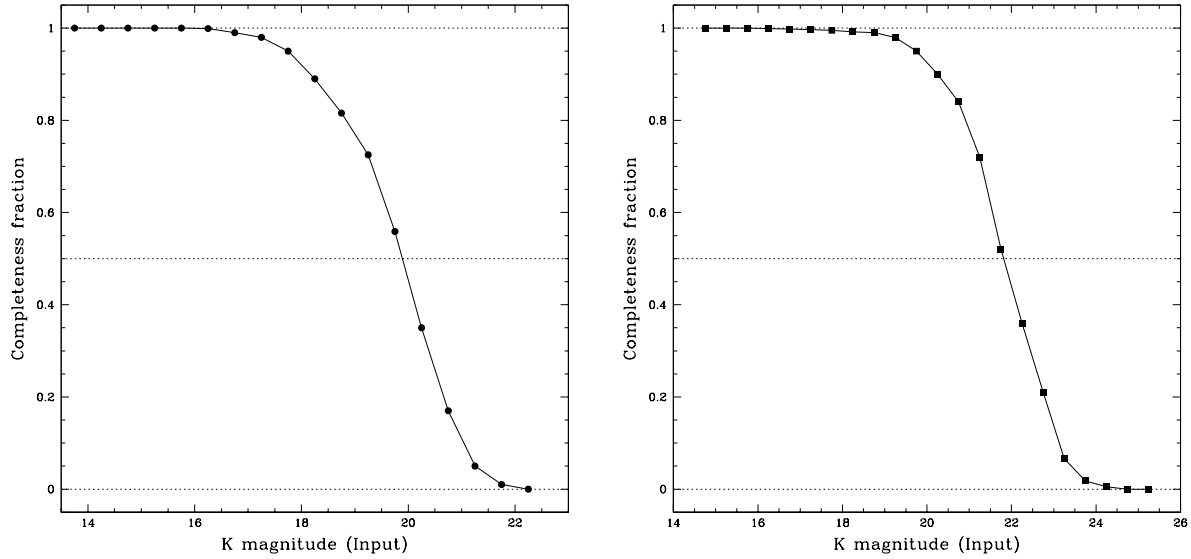

Figure 2. The completeness fraction for model galaxies for the AAT and NTT images (left and right panels, respectively) as a function of input magnitude, averaged over 20 fields. The mean 50% completeness limits is $K \sim 20$ for AAT images and $K \sim 21.5$ for the NTT sample.

some sources with a large deviations. These are caused by the proximity of a model object to a bright close source. We have checked the images and large errors such as these are avoided in the final output SExtractor catalogues.

The completeness fraction for model galaxies as a function of input magnitudes is shown in Figure 2 (Left panel) for the AAT images. These simulations have shown that the K_s–magnitude limit is $K_s \sim 20$. We have done similar analysis for the NTT images where the magnitude limit was $K_s \sim 21.5$ (See Figure 2, Right panel).

3 CLUSTER RICHNESS ASSOCIATED TO USS

In order to obtain an indication of the cluster richnesses associated to USS targets, we have calculated the Hill & Lilly (Hill & Lilly 1991) quantity. This is an Abell–type measurement, defined as the number of excess galaxies within a circle of of projected radius 0.5 Mpc (at the USS redshift), with magnitudes in the range m_1 to $m_1 + 3$, where m_1 is the typical magnitude of a USS radio galaxy. For comparison with previous studies we adopt a cosmolgy with $\Omega_M = 0.3$, $\Omega_\Lambda = 0.7$ and $H_0 = 100\,h$ kms^{-1} Mpc^{-1}, with $h = 0.7$.
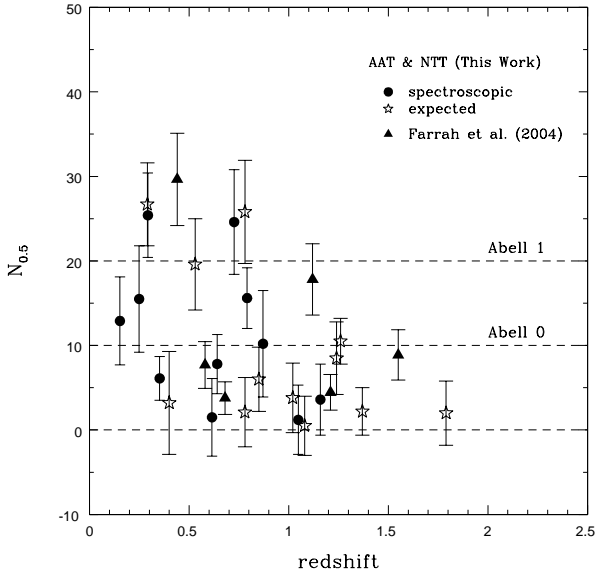
Figure 3. Values of the Hill & Lilly (Hill & Lilly 1991) quantity $N_{0.5}$ vs. redshift for the AAT and NTT sources. Solid circles represent data with spectroscopic redshift and stars represent data with expected redshift estimated from the $K - z$ Hubble Diagram (De Breuck et al. 2004). Solid triangles represents measurements from Hyperluminous Infrared Galaxies (HLIRGs) taken from Farrah et al. (2004). The horizontal dashed lines represent the conversion between $N_{0.5}$ and the traditional measure of Abell classes quoted in Farrah et al. (2004)

The average number of galaxies within the same magnitude range in the background was subtracted from the counts in the USS fields, calculated from an annular area region of the image at projected distances greater than ~ 1 Mpc distant from the USS targets. The uncertainties on $N_{0.5}$ are dominated by the uncertainties in the background subtraction. We calculated the error on $N_{0.5}$ from the $\sqrt{N}$ of this number. In Figure 3, we plot $N_{0.5}$ vs spectroscopic and expected redshift for USS images with limiting magnitudes fainter than $m_1 + 3$. We calculated the expected redshift for a USS radio source from the $K - z$ Hubble Diagram (De Breuck et al. 2002), using a photometry of 64 kpc radio–galaxy magnitudes. To calculate the 64 kpc metric apertures, we used the average correction for $z > 1$, $K_{64kpc} = K(8'') + 0.2$ (See for instance De Breuck et al. (2004)).

Some USS targets analyzed in this work show spectral signatures of QSOs. In this case, light from the AGN will dominate light from the host galaxy, making a direct measurement of m_1 impossible, m_1 is therefore estimated from the $K - z$ Hubble Diagram (De Breuck et al. 2002; De Breuck et al. 2004). We compare our determinations with the richness measurements of Hyperluminous Infrared Galaxies (HLIRGs) taken from Farrah et al. (2004) and we also plot the normalization between the value of $N_{0.5}$ and the traditional Abell richness as quoted in this work.

We find a variety of galaxy environments around our sample of USS targets. Most of the fields studied are compatible with being Abell class 0 richness clusters.

4 DISTRIBUTION OF GALAXIES WITH RESPECT TO THE USS RADIO AXIS

Röttgering et al. (1996), find an excess of companion galaxies up to ~ 80 kpc distance along the axes of the radio sources. Pentericci et al. (2001) reported a similar effect, finding nearby faint objects aligned with the direction of the main axis of the radio sources. All of these studies only deal with a few (< 30) companion galaxies. In this section we investigate the distribution of galaxies with respect to the USS radio axis.

In Figure 4 (Left panel) we show the distribution of the relative angle between the radius vector to companion galaxies with respect to the radio axis for galaxies with $15 < K_s < 20$ within $70 \ h^{-1}$ kpc of the USS targets, with spectroscopic or expected redshift $z \lesssim 1.5$. The distribution shows that the companion galaxies are predominantly located in the direction defined by the radio axis.

Following Sales & Lambas (2004) we may quantify the departure from an isotropy distribution defining two statistical tools. First, the ratio $f = N_{<30}/N_{>60}$, where $N_{<30}$ and $N_{>60}$ is the number of objects with $\Delta\phi < 30°$ and with $\Delta\phi > 60°$, respectively. For isotropy $f = 1$. And the second useful statistical measures of this anisotropy effect can be obtained by fitting a function to the ϕ distribution. We have adopted a double cosine function $N = A\cos(2\phi) + B$, and a linear fit $N = a_{lin}\phi + b$ where A and a_{lin} are the anisotropy parameter in each fit. For an isotropic distribution on $\Delta\phi$ we expect $A = a_{lin} = 0$. The resulting value is $f = 1.7 \pm 0.12$. Uncertainties were calculated based on 20 bootstrap re–sampling of the data. A suitable estimate of the significance is obtained by calculating f for a random distribution of USS position angles. From this test, we estimate that our results are significant at the 95 % confidence.

For the second test, the resulting values are $A = 3.2 \pm 0.6$ and $a_{lin} = -0.07 \pm 0.02$. We do not find great differences between the two model fits, however the double cosine function is less sensitive to noise fluctuations at the extremes due to poor number statistics.

In Figure 4 (Right panel) we plot the distribution of the orientation of companion galaxies with $15 < K_s < 20$ within $70 \ h^{-1}$ kpc of the USS targets with LAS $> 70 \ h^{-1}$ kpc and with LAS $< 70 \ h^{-1}$ kpc and with spectroscopic or expected redshifts $z \lesssim 1.5$. We find that the sample of USS targets with LAS $< 70 \ h^{-1}$ kpc are more aligned with the direction of the main axis of the radio galaxies that those with LAS $> 70 \ h^{-1}$ kpc. For the USS sample with LAS $< 70 \ h^{-1}$ kpc we obtain $f = 1.8 \pm 0.15$, $A = 4.2 \pm 0.25$ and $a_{lin} = -0.094 \pm 0.013$. And for the sample with LAS $> 70 \ h^{-1}$ kpc, $f = 1.55 \pm 0.18$, $A = 1.5 \pm 1.3$ and $a_{lin} = -0.05 \pm 0.05$ for the first and the second test respectively.

It is worth noting that given that K–band traces the evolved stellar populations (rather than R–band which may be obtain reflection nebulae and young or star-forming galaxies) our results indicate that being these evolved populations aligned with the radio structure, indicates that the radio orientation is linked to the large scale structure traced by galaxies with substantial evolution in these structures.

We can interpret this effect with a dynamical model for the formation of massive galaxies. West (1994) proposed a dynamical origin for the alignment effect. In this picture, powerful high redshift radio galaxies are assumed to rep-
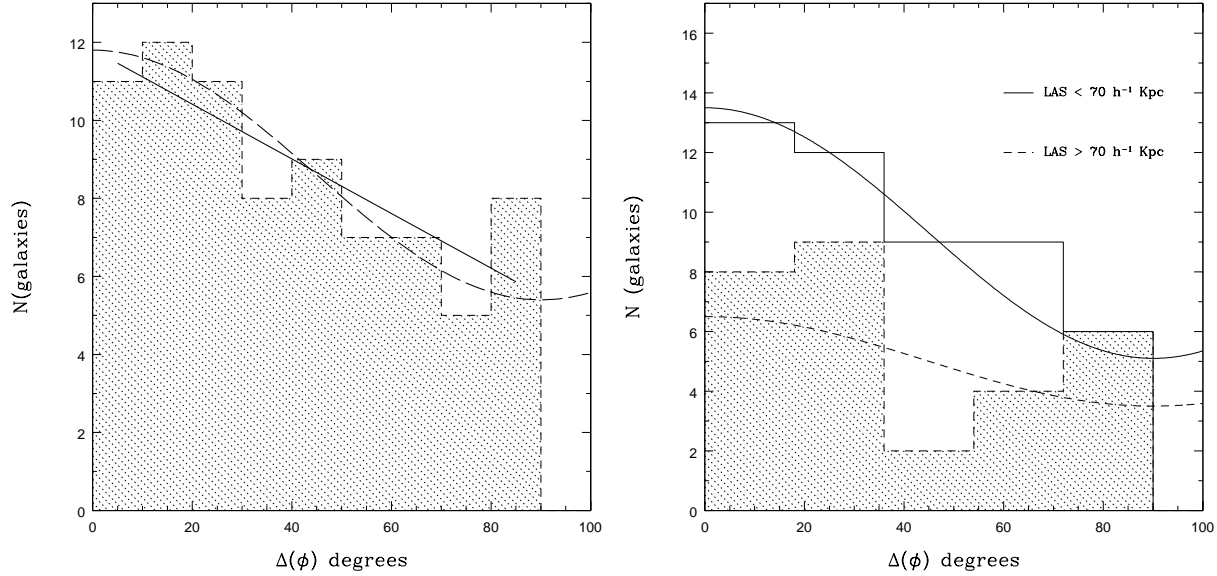
Figure 4. Left panel: distribution of the orientation of companion galaxies with $15 < K_s < 20$ within $70\ h^{-1}$ kpc of the USS targets, with respect to the radio axis. The solid line represent the linear fit relation and dashed lines is the double cosine function. Right panel: distribution of the orientation of companion galaxies with $15 < K_s < 20$ within $70\ h^{-1}$ kpc of the USS targets with LAS $> 70\ h^{-1}$ kpc (solid lines histogram) and LAS $< 70\ h^{-1}$ kpc (grey histogram) in all cases spectroscopic or expected redshift are $z \lesssim 1.5$.

resent an early stage in the formation of massive galaxies in the centers of rich clusters. Galaxy formation proceeds anisotropically by hierarchical merging of smaller protogalactic units along preferred directions, which are related to large–scale filamentary features in the surrounding mass distribution. As a consequence of this anisotropic formation process, these galaxies are quite prolate in shape. Infalling gas will quickly settle into an accretion disc whose angular momentum vector is aligned with the major axis of the galaxy mass distribution. If the radio jet emerges in the direction of this angular momentum vector, a natural consequence of such formation model is that one would expect companion galaxies to be preferentially located along the radio axis.

The model proposed here does not preclude the possibility that some fraction of the aligned light may have its origin in jet-induced star formation. In this case, this phenomena is only a second order effect which may act to enhance further the alignments with the radio axis.

5 CENTRAL CONCENTRATION INDICES

In this Section we have analyzed the USS galaxy morphology using an automated classification system based on central concentration of light. We used the concentration index (C), which is the fraction of an object's light contained in the central 30% of its area as measured in an ellipse aligned with the object and having the same axial ratio (see Abraham et al. (1994); Smail et al. (1997)).

The interpretation of the observed central light concentration indices has been assessed using galaxy model simulations, which is discussed in the next Subsection.

5.1 Simulations and the effects of seeing

We have done a set of galaxy image simulations in order to investigate the seeing effects degradation on central concentration indices. We created a series of model galaxies using the IRAF ARTDATA `mkobjects` task, similar to those analyzed in Section 2.4. The model objects were then convolved with a Gaussian function representing the PSF effects. SExtractor was run on the original and to the convolved model images to determine the differences between input and output values of C. We have done a similar analysis presented in Abraham et al. (1994). We plot the central concentration indices as a function of input magnitude for objects with $(4\ \text{PSF FWHM})^2 < area < (10\ \text{PSF FWHM})^2$ and those with $> (10\ \text{PSF FWHM})^2$ (See Figure 5). We note that small galaxies are largely affected by seeing. The lines represents the best fits between the input and recover positions on the diagram (Figure 5, left panel). On the other hand, we find that the PSF effect not affect the values of C when the projected area is substantially larger than the stellar seeing disk (Figure 5, right panel). Galaxies with projected areas smaller than $(4\ \text{PSF FWHM})^2$ were too strongly affected by seeing effects to be usefully classified.

5.2 Central Concentration indices properties

In Figure 6 we plot the corrected central concentration indices (C_1) vs expected redshift or spectroscopic redshift for the USS sample, assuming a correction $\Delta C = 0.1$, for galaxies with $(4\ \text{PSF FWHM})^2 < area < (10\ \text{PSF FWHM})^2$, where ΔC is the difference between input and recover positions. We compare our determinations with the C_1 vs z values of X–ray AGN selected sources in the Phoenix Deep Survey (Hopkins 1998; Georgakakis et al. 2004) and with determination obtain in the NICMOS Ultra Deep Field
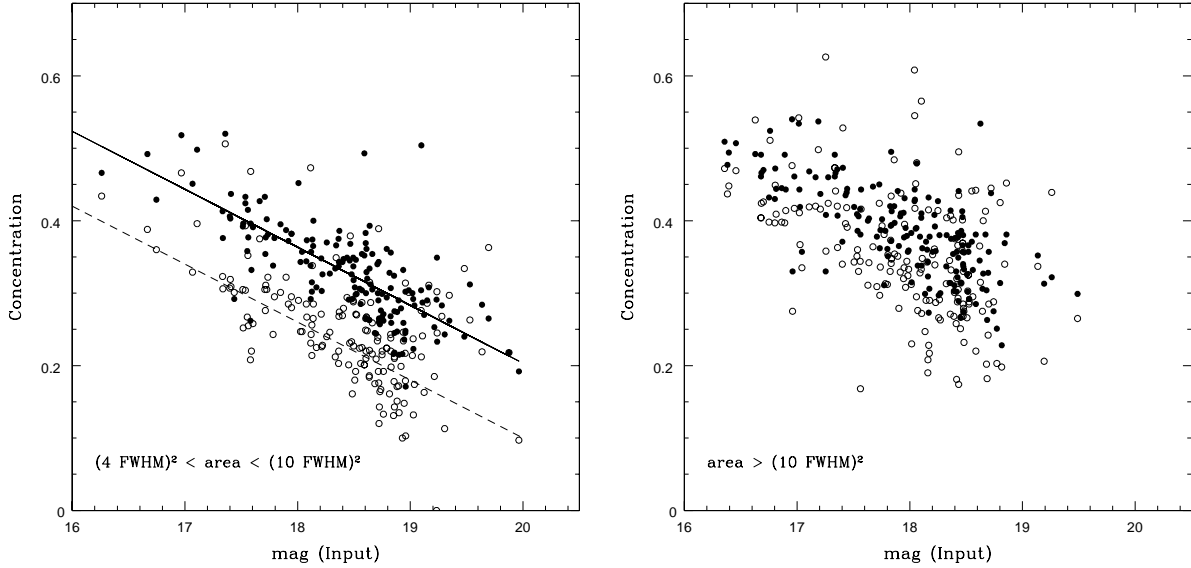
Figure 5. Left panel: Central concentration indices vs input magnitude from the simulation objects (See for instance Abraham et al. (1994, 1996). Filled circles and open represent input and output detected objects with $(4 \text{ PSF FWHM})^2 < area < (10 \text{ PSF FWHM})^2$. The lines represent the mean recovered position of objects due to the effects of seeing degradation. Right panel represent objects with $area > (10 \text{ PSF FWHM})^2$

(UDF)(Gwyn & Hartwick 2005). We use public K'–band images from Phoenix Deep Survey[2], we ran SExtractor with same parameters explained in Section 2.1. We identify the X–ray sources with available spectroscopic or photometric redshifts taken from Georgakakis et al. (2004). We have done the same analysis with the NICMOS (UDF) images [3] and then we cross-correlated our SExtractor catalogue with the public photometric redshift catalogue available in the NICMOS UDF web site. We have corrected the observed concentration indices as the same way as Section 5.1.

For this computation we don't measure the concentration indices of the QSOs in the sample, because they are dominated by the AGN light, making a direct measurement of C_1 impossible.

We find that at $z < 2$ our C_1 indices are similar with the concentration indices found in the field galaxies and X–ray selected sources. At $z > 2$ the USS sources are different from the general field population. They are highly concentrated in comparison with field galaxies at similar redshifts.

We believe that our USS sample represents the most massive star-forming systems, for a number of reasons. First, the concentration indices correlates with stellar mass (Conselice et al. 2005). Second, as reviewed in the introduction, at $z \gtrsim 1$ high redshift radio galaxies are $\gtrsim 2$ magnitudes brighter than normal galaxies at similar redshifts. This difference suggest that radio galaxies pinpoint the most massive systems out to the highest redshift. Third, a recently finished VLT large project (Kurk et al. 2000; Venemans et al. 2002, 2004, 2005; Miley et al. 2004) has found overdensities of > 20 spectroscopically Lyα and/or Hα companion galaxies, associated with galaxy

overdensities in all 5 targets studied.

We compare our richnesses measurements with concentration indices. In Figure 7 we plot the Hill & Lilly quantity $N_{0.5}$ vs central concentration indices C_1. We detect a weak, but significant, positive correlation between $N_{0.5}$ quantity and C_1. The Spearman rank correlation coefficients for this relations are $r = 0.65$ and $r = 0.71$ for the sample with spectroscopic and expected redshifts, respectively. For the whole redshift sample (spectroscopic and expected) we find $r = 0.68$.

A positive correlation between USS C_1 parameter and the environment $N_{0.5}$ value is expected given that the most massive USS hosts (those with larger C_1 values) are likely to be found in the densest galaxy environments.

6 CONCLUSIONS

We have analyzed different data sets corresponding to a sample of 70 Ultra Steep Spectrum (USS) radio sources selected from the 843 MHz Sydney University Molonglo sky Survey (SUMSS) and 1.4 GHz NRAO VLA Sky Survey (NVSS).

We have quantified galaxy excess around USS targets using an Abell–type measurement. We find that most of the USS fields studied are compatible with being Abell class 0 richness clusters.

A search for companion galaxies along the radio axis present a statistically significant result. The distribution of companion galaxies around USS radio sources show a pronounced tendency for such objects to be found in the direction defined by the radio axis, suggesting that they may be related to the presence of the USS radio sources. We interpret this effect with a model for the formation of radio galaxies via highly anisotropic mergers (West 1994). Maybe

---

[2] Data and further information available at http://www.atnf.csiro.au/people/ahopkins/phoenix/
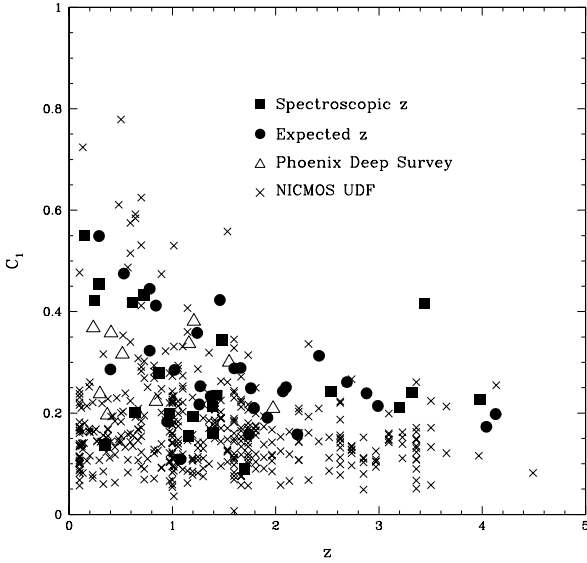[3] Data available at http://orca.phys.uvic.ca/ gwyn/MMM/nicmos.html

Figure 6. Corrected central concentration indices vs redshift measured for the AAT/NTT detected objects. Open squares represent data with spectroscopic redshift and filled circles represent data with expected redshift. Crosses are infrared photometric data taken from NICMOS Ultra Deep Field in the K'–band (Gwyn & Hartwick 2005). Open triangles are data taken from Phoenix Deep Field (Georgakakis et al. 2004).
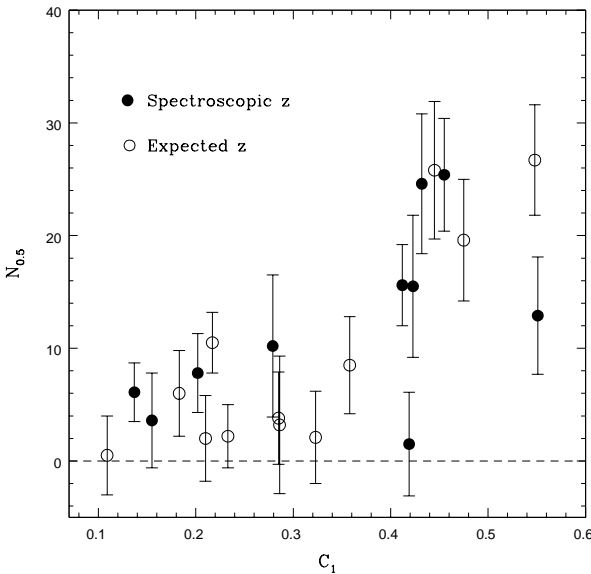

Figure 7. $N_{0.5}$ vs central concentration indices. Filled circles represent data with spectroscopic redshift and open circles represent data with expected redshift.

some fraction of the aligned galaxies may have its origin in jet-induced star formation.

We have also measure the central concentration of light of the USS sample and compare these to the values obtained for field galaxies and X–ray selected galaxies. We compare our richnesses determinations with concentration indices, and detected a weak, but significant, correlation between

$N_{0.5}$ and C_1 values. Also, we find that the higher redshift USS radio sources are more concentrated than field galaxies at similar redshifts. This difference suggest that USS radio galaxies trace the massive systems at high redshift.

7 ACKNOWLEDGEMENTS

REFERENCES

Abraham, R. G., Valdes, F., Yee, H. K. C., & van den Bergh, S. 1994, *ApJ*, 432, 75

Abraham, R. G., van den Bergh, S., Glazebrook, K., Ellis, R. S., Santiago, B. X., Surma, P., & Griffiths, R. E. 1996, *ApJS*, 107, 1

Bahcall, N. A., & Fan, X. 1998, *ApJ*, 504, 1

Bertin, E., & Arnouts, S. 1996, *A&AS*, 117, 393

Best, P. N. 2000, *MNRAS*, 317, 720

Best, P. N., Lehnert, M. D., Miley, G. K., & Röttgering, H. J. A. 2003, *MNRAS*, 343, 1

Blundell, K., Rawlings, S., Eales, S., Taylor, G., & Bradley, A. D. 1998, *MNRAS*, 295, 265

Bornancini, C. G., Martínez, H. J., Lambas, D. G., de Vries, W., van Breugel, W., De Breuck, C., & Minniti, D. 2004a, *AJ*, 127, 679

Bornancini, C. G., Martínez, H. J., Lambas, D. G., Le Floc'h, E., Mirabel, I. F., & Minniti, D. 2004b, *ApJ*, 614, 84

Chambers, K. C., Miley, G. K., van Breugel, W. J. M., Bremer, M. A. R., Huang, J.-S., & Trentham, N. A. 1996a, *ApJS*, 106, 247

Chambers, K. C., Miley, G. K., van Breugel, W. J. M., & Huang, J.-S. 1996b, *ApJS*, 106, 215

Conselice, C. J., Blackburne, J. A., & Papovich, C. 2005, *ApJ*, 620, 564

Croft, S., Kurk, J., van Breugel, W., Stanford, S. A., de Vries, W., Pentericci, L., Röttgering, H. 2005, *AJ*, 130, 867

De Breuck, C., van Breugel, W., Stanford, S. A., Röttgering, H., Miley, G., & Stern, D. 2002, *AJ*, 123, 637

De Breuck, C., Hunstead, R. W., Sadler, E. M., Rocca-Volmerange, B., & Klamer, I. 2004, *MNRAS*, 347, 837

De Breuck, C., Klamer, I., Johnston, H., Hunstead, R. W., Bryant, J., Rocca-Volmerange, B., Sadler, E. M., *MNRAS*, in press (astro-ph/0511169)

Farrah, D., Geach, J., Fox, M., Serjeant, S., Oliver, S., Verma, A., Kaviani, A., & Rowan-Robinson, M. 2004, *MNRAS*, 349, 518

Georgakakis, A., Hopkins, A. M., Afonso, J., Sullivan, M., Mobasher, B., & Cram, L. E. 2004, *MNRAS*, 354, 127

Gwyn, S. D .J , & Hartwick, F. D .A 2005, *AJ*, submitted

Hill, G. J. & Lilly, S. J. 1991, *ApJ*, 367, 1

Hopkins, A. M. 1998, Ph.D. Thesis,

Jarvis, M. J., Rawlings, S., Eales, S., Blundell, K. M., Bunker, A. J., Croft, S., McLure, R. J., & Willott, C. J. 2001, *MNRAS*, 326, 1585

Knopp, G. P. & Chambers, K. C. 1997, *ApJS*, 109, 367

Kurk, J. D., et al. 2000, *A&A*, 358, L1

Kurk, J. D., Pentericci, L., Overzier, R. A., Röttgering, H. J. A., & Miley, G. K. 2004a, *A&A*, 428, 817

Kurk, J. D., Pentericci, L., Röttgering, H. J. A., & Miley, G. K. 2004b, *A&A*, 428, 793

Lilly, S & Longair, M. 1984, *MNRAS*, 211, 833

Miley, G. K., et al. 2004, *Nature*, 427, 47

Pentericci, L., Röttgering, H. J. A., Miley, G. K., Carilli, C. L., & McCarthy, P. 1997, *A&A*, 326, 580

Pentericci, L., et al. 2000, *A&A*, 361, L25

Pentericci, L., McCarthy, P. J., Röttgering, H. J. A., Miley, G. K., van Breugel, W. J. M., & Fosbury, R. 2001, *ApJS*, 135, 63

Pentericci, L., Kurk, J. D., Carilli, C. L., Harris, D. E., Miley, G. K., Röttgering, H. J. A. 2002, *A&A*, 396, 109

Rocca-Volmerange, B., Le Borgne, D., De Breuck, C., Fioc, M., & Moy, E. 2004, *A&A*, 415, 931

Röttgering, H. J. A., Lacy, M., Miley, G. K., Chambers, K. C., & Saunders, R. 1994, A&AS, 108, 79

Röttgering, H. J. A., West, M. J., Miley, G. K., & Chambers, K. C. 1996, *A&A*, 307, 376

Sales, L., & Lambas, D. G. 2004, *MNRAS*, 348, 1236

Smail, I., Dressler, A., Couch, W. J., Ellis, R. S., Oemler, A. J., Butcher, H., & Sharples, R. M. 1997, *ApJS*, 110, 213

Venemans, B. P., et al. 2002, *ApJ*, 569, L11

Venemans, B. P., et al. 2004, *A&A*, 424, L17

Venemans, B. P., et al. 2005, *A&A*, 431, 793

West, M. J. 1994, *MNRAS*, 268, 79

Table 1. NTT Sample characteristics. Designation in IAU J2000 format, J2000 coordinates of the $K-$band identification, the spectral index α_{843}^{1400}, position angle of the radio structure determined from the ATCA maps, largest radio size, the K counterpart magnitude, the Hill & Lilly quantity $N_{0.5}$, the corrected central concentration, the spectroscopic and the expected redshift and the 1.5 σ limiting magnitude per field.

(1) Name	(2) α_{843}^{1400}	(3) PA °	(4) LAS h^{-1}kpc	(5) K−mag. MAG_BEST	(6) $N_{0.5}$	(7) C_1	(8) z spectroscopic	(9) z expected	(10) Limiting mag. 1.5σ
NVSS J002738−323501	-1.59±0.20	23	269.1	18.06±0.06	2.0±3.8	0.210	...	1.79	21.4
NVSS J011606−331241	-1.70±0.20	...	<20.7	18.27±0.06	6.1±7.6	0.137	0.352±0.001	1.50	21.4
NVSS J014413−330457	-0.82±0.27	97	228.6	18.55±0.08	...	0.239	...	2.88	21.5
NVSS J015436−333425	-1.59±0.12	...	<35.5	19.67±0.12	...	...	...	1.74	21.1
NVSS J202945−344812	-1.25±0.10	167	112.0	19.42±0.02	...	...	1.497±0.002[b]	1.14	21.4
NVSS J204420−334948[a]	-1.60±0.11	15	...	...	...	...	...	...	21.3
NVSS J230035−363410	-1.67±0.14	...	<27.0	20.50±0.22	...	0.173	...	4.04	21.1
NVSS J230123−364656	-1.61±0.14	...	<31.7	19.63±0.14	...	0.211	3.220±0.002	2.62	21.5
NVSS J230527−360534[a]	-1.64±0.10	...	...	...	...	...	...	...	21.1
NVSS J230954−365653	-1.15±0.18	25	...	19.75±0.15	...	0.198	...	6.27	21.1
NVSS J231144−362215	-1.32±0.12	69	92.4	20.20±0.17	...	0.243	2.531±0.002	4.45	21.6
NVSS J231338−362708	-1.50±0.12	123	10.7	19.10±0.10	...	0.089	1.838±0.002	2.93	21.4
NVSS J231726−371443	-1.23±0.09	19	80.3	19.07±0.10	...	...	...	1.99	21.2
NVSS J231727−352606[a]	-1.33±0.09	124	21.2	...	...	...	3.874±0.002	...	21.5
NVSS J232001−363246	-2.01±0.16	...	<28.8	19.79±0.17	...	0.198	1.483±0.001	4.13	21.6
NVSS J232100−360223	-1.77±0.14	...	31.3	20.00±0.20	...	0.240	3.320±0.005	3.96	21.6
NVSS J232219−355816[a]	-1.87±0.10	149	...	...	...	...	...	...	21.5
NVSS J233558−362236	-1.24±0.16	148	209.5	16.52±0.01	15.5±3.6	0.412	0.791±0.001	0.76	21.4
NVSS J234137−342230[a]	-1.55±0.15	...	...	...	...	...	...	...	21.2
NVSS J235137−362632[a]	-1.62±0.11	10	...	...	...	...	...	...	21.0

[a] Radio position.
[b] QSO.

Table 2. Same as table 1 for the AAT USS Sample.

(1) Name	(2) α_{843}^{1400}	(3) PA °	(4) LAS h^{-1}kpc	(5) K−mag. MAG_BEST	(6) $N_{0.5}$	(7) C_1	(8) z spectroscopic	(9) z expected	(10) Limiting mag. 1.5σ
NVSS J002001−333408	-1.38±0.13	38	71.0	17.91±0.08	...	0.423	continuum[a]	1.46	20.0
NVSS J002112−321208	-1.66±0.13	...	<27.8	19.25±0.19	...	0.261	...	2.69	20.0
NVSS J002131−342225	-1.57±0.15	116	34.2	15.29±0.01	15.5±6.3	0.423	0.249±0.001	0.37	20.0
NVSS J002352−332338	-1.10±0.13	79	221.3	19.20±0.25	...	...	...	1.98	19.8
NVSS J002359−325756	-1.69±0.09	94	12.1	18.39±0.12	...	0.158	...	2.21	20.0
NVSS J002402−325253	-1.74±0.10	4	22.1	19.07±0.23	...	...	2.043±0.002	2.57	20.0
NVSS J002415−324102	-1.78±0.10	...	<28.5	...	...	...	...	...	19.8
NVSS J002427−325135	-1.54±0.11	171	38.9	17.19±0.09	2.2±2.7	0.233	continuum	1.37	20.3
NVSS J011032−335445	-1.52±0.16	23	<29.6	18.67±0.16	...	0.158	continuum	1.74	20.0
NVSS J011643−323415	-0.93±0.33	121	250.8	18.05±0.13	...	0.289	...	1.66	20.0
NVSS J014529−325915	-1.32±0.15	41	67.4	15.80±0.01	19.6±5.4	0.475	...	0.53	20.0
NVSS J015232−333952	-1.32±0.09	7	52.6	16.26±0.02	1.5±4.6	0.419	0.6148±0.001	0.60	20.5
NVSS J015324−334117	-1.23±0.15	91	49.2	14.51±0.01	12.9±5.2	0.551	0.1525±0.0004	0.22	20.2
NVSS J015418−330150	-1.23±0.15	...	<29.4	...	...	...	...	...	20.5
NVSS J015544−330633	-1.14±0.11	115	105.5	16.93±0.05	1.2±4.1	...	1.048±0.002[b]	0.94	20.0
NVSS J021308−322338	-1.42±0.11	...	26.2	19.14±0.22	...	0.296	3.98±0.001	3.27	19.4
NVSS J021359−321115	-1.29±0.15	...	<35.6	17.89±0.07	...	0.288	...	1.60	20.0
NVSS J021545−321047	-1.59±0.10	98	42.6	19.20±0.22	...	...	...	2.44	20.0
NVSS J021716−325121	-1.52±0.12	44	24.2	18.75±0.20	...	0.213	1.384±0.002	1.76	20.0
NVSS J030639−330432	-1.70±0.10	...	<29.0	17.88±0.11	...	0.193	1.201±0.001	1.42	20.2
NVSS J202026−372823	-1.34±0.10	...	<29.6	18.56±0.15	...	0.235	1.431±0.001	1.67	20.2
NVSS J202140−373942	-1.34±0.14	29.1	45.8	15.20±0.01	3.2±6.1	0.286	...	0.40	19.6
NVSS J202518−355834	-1.55±0.11	...	<35.5	18.43±0.10	...	0.249	...	1.76	20.0
NVSS J202856−353709	-1.07±0.10	129	186.6	16.60±0.04	2.1±4.2	0.323	continuum	0.78	20.0
NVSS J204147−331731	-1.35±0.13	168	23.1	16.86±0.05	10.2±6.3	0.279	0.871±0.001	0.84	20.1
NVSS J213510−333703	-1.46±0.11	15	<20.4	...	...	...	2.518±0.001	2.11	19.0
NVSS J225719−343954	-1.69±0.09	...	30.5	16.53±0.02	24.6±6.2	0.432	0.726±0.001	0.70	19.8
NVSS J230203−340932	-1.31±0.14	91	148.6	17.34±0.07	3.6±4.2	0.155	1.159±0.001	2.14	20.4
NVSS J230404−372450	-1.24±0.12	126	181.5	17.40±0.10	0.5±3.5	0.109	continuum	1.08	20.4
NVSS J230822−325027	-1.68±0.11	141	9.9	18.47±0.10	...	0.251	...	2.10	20.0
NVSS J230846−334810	-1.07±0.10	114	110.4	16.97±0.02	25.8±6.1	0.445	continuum	0.78	20.1
NVSS J231016−363624	-1.48±0.13	3	85.0	14.60±0.05	26.7±4.9	0.549	...	0.29	20.2
NVSS J231229−371324	-1.40±0.12	161	32.1	17.31±0.08	10.5±2.7	0.217	continuum	1.26	20.4
NVSS J231311−361558	-0.54±0.14	48	367.0	17.49±0.08	8.5±4.3	0.358	...	1.24	20.5
NVSS J231317−352133	-1.35±0.13	102	33.8	19.14±0.25	...	...	...	2.24	20.0
NVSS J231335−370609	-1.21±0.11	...	<23.6	18.63±0.18	...	0.191	...	1.92	20.0
NVSS J231341−372504	-1.23±0.18	155	250.3	16.97±0.07	6.0±3.8	0.183	continuum	0.95	20.0
NVSS J231357−372413	-1.58±0.10	47	11.8	16.00±0.03	...	0.161	1.393±0.001	0.76	20.4
NVSS J231402−372925	-1.37±0.08	48	22.2	18.69±0.15	...	0.416	3.450±0.005	2.15	20.0
NVSS J231459−362859	-1.16±0.11	16	55.2	19.15±0.15	...	0.313	...	2.42	20.0
NVSS J231519−342710	-1.41±0.11	106	119.8	18.10±0.13	...	0.200	0.970±0.001	1.41	20.1
NVSS J232014−375100	-1.11±0.13	128	262.1	17.60±0.10	...	0.253	...	1.27	20.0
NVSS J232058−365157	-1.38±0.09	...	29.6	18.65±0.12	...	0.344	...	2.28	20.0
NVSS J232322−345250	-1.19±0.15	...	31.0	17.07±0.08	3.8 ±4.1	0.285	continuum	1.02	20.1
NVSS J232602−350321	-0.94±0.24	140	46.8	14.23±0.11	25.4±5.0	0.455	0.293±0.001	0.27	19.8
NVSS J232651−370909	-1.56±0.10	...	<21.6	19.16±0.10	...	0.214	...	2.99	20.2
NVSS J232956−374534	-1.53±0.10	...	<35.0	19.06±0.21	...	0.243	...	2.07	20.0
NVSS J233729−355529	-1.33±0.09	72	43.9	...	...	...	...	...	20.0
NVSS J234145−350624	-1.30±0.08	...	<24.0	15.94±0.04	7.8±3.5	0.202	0.641±0.001	0.60	20.0
NVSS J234904−362451	-1.31±0.10	137	56.3	17.63±0.14	3.8±2.5	...	1.520±0.003[b]	1.33	20.5

[a] Objects with continuum features, no emission lines.
[b] QSO.